Computers and Geotechnics 176 (2024) 106703

Contents lists available at ScienceDirect

Computers and Geotechnics

journal homepage: www.elsevier.com/locate/compgeo

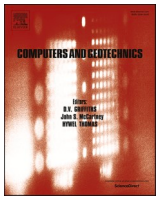

Research Paper

Instability mechanisms in partially saturated coarse-grained soils: Implications for rainfall-induced flowslides

G.M. Rotisciani [a], F. Novelli [c], A. Desideri [b], A. Amorosi [b,*]

[a] Dipartimento di Ingegneria, Università degli Studi Niccolò Cusano, Via Don Carlo Gnocchi 3, 00166 Rome, Italy
[b] Dipartimento di Ingegneria Strutturale e Geotecnica, Università di Roma La Sapienza, Via Eudossiana 18, 00184 Rome, Italy
[c] Formerly Dipartimento di Ingegneria Strutturale e Geotecnica, Università di Roma La Sapienza, Via Eudossiana 18, 00184 Rome, Italy

ARTICLE INFO

To the memory of our colleague and friend Augusto Desideri.

Keywords:
Partial saturation
Wetting
Local stability
Flowslides
Infinite slope
Constitutive modelling

ABSTRACT

This paper deals with the wetting-induced instabilities that can occur in unsaturated shallow slopes and cause the evolution of slides into flowslides. In particular, it examines the instability phenomena that manifest in the unsaturated regime prior to shear failure, focusing on the triggering mechanism and predisposing factors. A theoretical index to capture instability initiation is derived in a general form that is valid for all single-surface isotropic hardening plasticity models, regardless of the assumption on the flow rule and the type of perturbation applied. The criterion is then specialised to the case of the WR2-Unsat model and used to monitor the stability of a soil element belonging to an ideal infinite slope during wetting processes. The results of the parametric study suggest that particular attention should be paid to relatively steep slopes with a shallow cover of no more than a couple of metres, consisting of highly collapsible and/or compressible coarse-grained soils with a low fine fraction susceptible to liquefaction.

1. Introduction

Rainfall induced landslides are one of the most recurrent and destructive geohazards worldwide, and their frequency has increased significantly over time. Indeed, in recent years, several catastrophic rainfall-induced landslides have been recorded in many regions of the world as, for example, Italy (Salciarini et al., 2006; Cascini et al., 2008; Montrasio and Valentino, 2008; Damiano et al., 2012; Cevasco et al., 2013; Sorbino and Nicotera, 2013; Zizioli et al., 2013); Switzerland (Laloui et al., 2009; Springman et al., 2013); China (Dai et al., 1999; Fuchu et al., 1999; Yang et al., 2020); Vietnam (Nguyen et al., 2020).

These phenomena can exhibit very different kinematics depending on the material involved in the unstable process. In coarse-grained soils, landslides generally develop as first slope failures with velocities much higher than those observed in fine-grained deposits. The high velocities are due to the instability of the soil skeleton in totally or partially undrained conditions, which causes the evolution of slides into flowslides (Chu et al., 2003; Picarelli et al., 2008, Sorbino and Nicotera, 2013). In shallow unsaturated slopes, rainfall infiltration, which in general can cause significant deformations and losses of shear strength (Oh and Vanapalli, 2010; Rotisciani et al., 2017; Hou et al., 2019; Weng et al., 2019; Lalicata et al., 2020; Wu et al., 2020), is the most common triggering factor for landslides.

In recent years, great efforts have been made to improve our understanding of the main mechanisms governing the triggering and propagation of flowslides (see review by Cuomo, 2020). An interesting approach is the one proposed by Chen and Buscarnera (2022), who presented a spatially condensed modelling framework that allows for straightforward use of soil constitutive models in the analysis of the transition from triggering to runout of flowslides. An alternative approach, mostly applied to landslide propagation problems, is the use of Smoothed Particles Hydrodynamics (SPH) models (Bui et al., 2008; Pastor et al., 2009; Bui and Nguyen, 2021; Lian et al., 2022; Tayyebi et al., 2022). The latter are developed in a continuum mechanics framework and well reproduce the strong coupling between the solid skeleton and the fluids filling its voids, which affects properties such as runout and velocity of the flowslides.

The work presented here focuses only on the triggering phase, investigating the causes of the instability and modelling its activation. Understanding how and when the unstable process occurs is crucial for the correct assessment of slope safety.

The evolution into flowslides is often attributed to the unstable behaviour of the soil under undrained loading conditions. A significant drop in shear strength can lead to a transition from solid-like to fluid-like

* Corresponding author.
E-mail addresses: giada.rotisciani@unicusano.it (G.M. Rotisciani), augusto.desideri@uniroma1.it (A. Desideri), angelo.amorosi@uniroma1.it (A. Amorosi).

https://doi.org/10.1016/j.compgeo.2024.106703
Received 27 February 2024; Received in revised form 24 June 2024; Accepted 25 August 2024
Available online 7 September 2024

behaviour, i.e. static liquefaction of the deposit (Buscarnera and di Prisco, 2013; Cuomo et al., 2019; Ng et al., 2022). Two scenarios can be distinguished for the initiation and evolution of slides into flowslides. The first is the most common and involves the occurrence of shear failure under drained conditions (Wang and Sassa, 2001, 2003, Okura et al., 2002; Damiano, 2003; Moriwaki et al., 2004; Cascini et al., 2005; Olivares and Damiano, 2007; Pirone et al., 2015; Comegna et al., 2016;). Failure usually occurs in the lower part of the potentially unstable soil layer when the soil is already fully saturated. Such failure is due to the reduction in available shear strength caused by the increase in pore water pressure. Sliding of the soil mass can lead to the build-up of positive excess pore water pressures and, consequently, to the occurrence of static liquefaction in the deformed portions of the deposit. For this to occur, it is necessary that *i*) the movement is rapid, *ii*) the soil layer consists of coarse-grained soil with a fine fraction that reduces the permeability and justify the build-up of excess pore water pressures; *iii*) the soil exhibits a tendency to liquefy.

The second scenario implies the static liquefaction being a consequence of a previous instability activated by suction removal (Picarelli et al. 2008; Buscarnera and di Prisco, 2013; Rotisciani et al., 2019; Cuomo et al., 2021). In fact, in highly compressible unsaturated soils the loss of suction can cause a sudden volumetric collapse, which in turn leads to uncontrolled saturation of the material. In this case, the unstable transition from unsaturated to fully saturated conditions is the triggering factor for static liquefaction and thus for the evolution of landslides into flowslides.

This paper investigates this second mechanism, focusing in particular on the early instability that occurs in the unsaturated regime. The study has two main objectives.

The first is to provide an analytical criterion that allows i) to monitor the stability of the soil response under loading and wetting processes, detecting the onset of any instability, ii) to identify the factors that contribute the most to the loss of control. Here the stability criterion is derived following the strategy proposed in Buscarnera et al. (2011) and Buscarnera (2014) in the context of plasticity theory. This is based on the identification of the set of scalar variables that reveal the loss of definition of the plastic multiplier under specific loading conditions. The choice and evaluation of these variables depend on the constitutive assumptions adopted to describe the soil behaviour which, in turn, affects the accuracy and reliability of the analysis results. In the following, reference is made to the WR2-Unsat model, a versatile single-surface hardening plasticity model that satisfactorily reproduces the key hydro-mechanical features of fully and partially saturated soils, also taking into account the effects of bond degradation (Boldini et al., 2019; Rotisciani et al., 2021; Rotisciani et al., 2023). The shape of the yield and plastic potential surfaces can vary depending on the class of material considered. The flow rule can be associated or not, depending on the shape of the two surfaces. The very flexible formulation allows the model to capture soil instabilities in both unsaturated and fully saturated regimes.

The second objective is to verify the ability of the above criterion to capture the occurrence of wetting instabilities in an ideal infinite slope. At this scope, the effects of water infiltration are evaluated with respect to a single soil element located at the base of the shallow cover, thus neglecting, for the sake of simplicity, any variation in the spatial distribution of the stress–strain components within the soil layer. This approach facilitates the analysis of the failure mechanism by establishing a direct correlation between changes in material state and loss of suction. The results of the parametric study, carried out by modifying one by one the soil properties and the slope geometry within the ranges typically observed in natural deposits involved in flowslides, show the activation of the unstable process and identify which factors contribute the most to instability.

The main novelties of this work are therefore: *i*) the application of the strategy proposed by Buscarnera (2014) to a recently formulated constitutive model that reproduces well the main features of the experimentally observed unsaturated soil response. *ii*) The discussion and identification of material stability in a more flexible and general way as compared to what was done in Rotisciani et al. (2021). In fact, in this work we generalise the instability criterion identified in the past only with reference to specific perturbation conditions, analytically deriving a formulation valid for any type of applied hydro-mechanical perturbation, regardless of the flow rule assumed. *iii*) The application of the criterion to an idealised, though realistic, slope stability problem, consisting of an infinite unsaturated slope exposed to rainfall events, whose behaviour is described with reference to a soil element located at the base of the shallow unstable layer.

The paper is organized as follows. The following section presents the strategy employed to define, in a general form, suitable indexes to identify unstable processes. After a brief description of the constitutive laws adopted for describing the hydro-mechanical soil behaviour, the stability indexes are then specialized to the selected constitutive model (Section 3). The effects of water infiltration on slope stability are investigated numerically for a single element belonging to an ideal infinite slope in Sections 4 and 5. Finally, concluding remarks are given in section 6.

2. The general framework for defining stability criteria

The analysis of soil stability during water infiltration requires the definition of suitable indexes to identify unstable conditions. At this scope, the approach adopted here is that originally proposed in the framework of plasticity theory by Buscarnera et al. (2011) and extended to partial saturation conditions by Buscarnera (2014). Such a strategy is based on the idea that, within the classical elasto-plastic framework, the loss of uniqueness of the incremental response can be related to the evolution of the hardening modulus. Indeed, critical values of the plastic hardening modulus can be associated with the loss of positive definiteness of the second order work (Bigoni and Hueckel, 1991a, 1991b; Hueckel and Maier, 1977; Maier and Hueckel, 1979). All the above works neglect the crucial role of the control conditions on the material stability, considering it as an intrinsic property of the current state of the soil. To overcome this limitation, Buscarnera et al. (2011) proposed a new family of scalar functions that act as a sort of generalised hardening moduli governing the mechanical response under mixed stress–strain control. Such indices depend on the current state of the material and the control conditions imposed in the test. This strategy has been successfully used to capture the occurrence of diffuse unstable phenomena such as static liquefaction, localised failure such as shear banding (Mihalache and Buscarnera, 2014) and to evaluate the influence of suction on the bifurcation potential (Buscarnera, 2014). More in detail, Buscarnera (2014) adopted this theory to identify the elements of hydro-mechanical coupling that affect the potential for a loss of uniqueness of the incremental response. To simplify the mathematical derivation of the bifurcation conditions, the analysis was restricted to isotropic stress paths, assuming associated flow rule and neglecting any soil deformations within the elastic domain. The Author inspected the implications on soil stability of the constitutive assumptions and of the different forms of coupling between plasticity and state of saturation.

In this work, the above approach is extended to more general conditions, including loading paths characterised by changes in both stress invariants and/or hydraulic conditions, while also considering non-associated flow rule. The stability indexes are derived in a general form with reference to a specific class of constitutive models characterized by: i) single-surface elastic-isotropic hardening plasticity formulation; ii) non-associated flow rule; and iii) non-hysteretic uncoupled retention behaviour. All the models belonging to this class satisfies the following assumptions:

$$f = f(\boldsymbol{\sigma}', \Psi) \tag{1}$$

$$g = g(\boldsymbol{\sigma}', \widehat{\Psi}) \tag{2}$$

$$\Psi = \Psi(\varepsilon^{p}, S_r) \tag{3}$$

$$S_r = S_r(s) \tag{4}$$

Where f indicates the yield locus, $\boldsymbol{\sigma}'$ is the Bishop's effective stress tensor defined as: $\boldsymbol{\sigma}' = \boldsymbol{\sigma} + S_r s\boldsymbol{\delta}$ where $\boldsymbol{\sigma}$ is the total stress tensor coincident with the net stress tensor assuming zero pore air pressure u_a, S_r is the degree of saturation, s is the matrix suction equal to the difference between u_a and the pore water pressure u_w, $\boldsymbol{\delta}$ is the Kronecker operator. Ψ is the hardening scalar variable that controls the dimension of the yield surface, and evolves with plastic strains $\boldsymbol{\varepsilon}^p$ and S_r. g defines the plastic potential function depending on the effective stress tensor and the dummy variable $\widehat{\Psi}$, the latter identifying the dimension of the g-locus passing through the current stress state. The retention behaviour is described by a unique analytical expression linking the degree of saturation and the suction.

In this study, the conditions leading to the loss of uniqueness and existence of the incremental response are inspected with reference to the two sets of control variables: $\boldsymbol{\sigma}$ and s or $\boldsymbol{\sigma}$ and w, being w the water content. The first set describes loading tests performed under constant suction, namely under drained conditions, and wetting tests carried out by gradually reducing suction level under constant total stress. The second set is representative of water-undrained loading tests and wetting paths performed by increasing water content under constant total stresses.

In the first case, the plastic multiplier $\dot{\gamma}$ takes the form (see Appendix A):

$$\dot{\gamma} = \frac{1}{H}\left\langle \frac{\partial f}{\partial \boldsymbol{\sigma}'}^{T} \dot{\boldsymbol{\sigma}} + \frac{\partial f}{\partial s}\dot{s} \right\rangle \tag{5}$$

Where $\langle\rangle$ are the McCauley brackets, $\dot{\boldsymbol{\sigma}}$ is the total stress tensor increment, $\dot{s}$ is the increment of suction, $\partial f/\partial \boldsymbol{\sigma}'$and $\partial f/\partial s$ are the partial derivatives of the yield surface with respect to $\boldsymbol{\sigma}'$ and s, respectively. $\partial f/\partial s$ is defined as follows:

$$\frac{\partial f}{\partial s} = \frac{\partial f}{\partial \boldsymbol{\sigma}'}^{T}\left(\frac{\partial S_r}{\partial s}s + S_r\right)\boldsymbol{\delta} + \frac{\partial f}{\partial \Psi}\frac{\partial \Psi}{\partial S_r}\frac{\partial S_r}{\partial s} \tag{6}$$

Where $\partial f/\partial \Psi$ is the partial derivatives of the yield surface with respect to Ψ, $\partial \Psi/\partial S_r$ represents the partial derivative of the internal variable with respect to S_r, $\partial S_r/\partial s$ defines the variation of the degree of saturation with suction. Finally, H is the hardening modulus defined as follows:

$$H = -\frac{\partial f}{\partial \Psi}\frac{\partial \Psi}{\partial \boldsymbol{\varepsilon}^p}\frac{\partial g}{\partial \boldsymbol{\sigma}'} \tag{7}$$

Where $\partial \Psi/\partial \boldsymbol{\varepsilon}^p$ is the partial derivative of the hardening variable with respect to $\boldsymbol{\varepsilon}^p$ and $\partial g/\partial \boldsymbol{\sigma}'$ is the partial derivative of the plastic potential with respect to $\boldsymbol{\sigma}'$.

According to Eq. (5), the plastic strains are activated by loading and/or wetting processes provided that the term $(\partial f/\partial \boldsymbol{\sigma}')^{T}\dot{\boldsymbol{\sigma}} + (\partial f/\partial s)\dot{s}$ is greater than 0. In these cases, the plastic multiplier is no longer defined when:

$$H \leq 0 \tag{8}$$

This simple analytical result discloses that, under the control of suction and net stresses, *i*) it is sufficient to check the sign of the hardening modulus to assess the uniqueness and existence of the incremental response; *ii*) no instability can take place in the hardening regime.

In the second case, the plastic multiplier is expressed as follows (see Appendix B):

$$\dot{\gamma} = \frac{1}{H - H_w}\left\langle \overline{n}_{\sigma}^{T}\dot{\boldsymbol{\sigma}} + \frac{1-n}{n}\overline{n}_{S_r}\dot{e_w} \right\rangle \tag{9}$$

Where n is the porosity, $\dot{e_w}$ is the increment in the water ratio being e_w the ratio between the water and solid volumes, $\overline{n}_{\sigma}$ and $\overline{n}_{S_r}$ are defined by the following expressions:

$$\overline{n}_{\sigma} = \frac{\partial f}{\partial \boldsymbol{\sigma}'} + \frac{S_r}{n}\overline{n}_{S_r}(\boldsymbol{C}^e\boldsymbol{\delta}) \tag{10}$$

$$\overline{n}_{S_r} = \frac{\partial f/\partial S_r}{\left[1 - \frac{S_r}{n}C^e_{pp}\left(s + \frac{\partial s}{\partial S_r}S_r\right)\right]} \tag{11}$$

being $\boldsymbol{C}^e$ the elastic compliance matrix, C^e_{pp} the elastic compressibility: $C^e_{pp} = (\boldsymbol{C}^e\boldsymbol{\delta})^{T}\boldsymbol{\delta}$, $\partial f/\partial S_r$ the partial derivative of the yield locus with respect to S_r:

$$\frac{\partial f}{\partial S_r} = \frac{\partial f}{\partial \boldsymbol{\sigma}'}^{T}\left(\frac{\partial s}{\partial S_r}S_r + s\right)\boldsymbol{\delta} + \frac{\partial f}{\partial \Psi}\frac{\partial \Psi}{\partial S_r} \tag{12}$$

and H_w a sort of critical hardening modulus taking the form:

$$H_w = \overline{n}_{S_r}\frac{S_r}{n}\frac{\partial g}{\partial \boldsymbol{\sigma}'}\boldsymbol{\delta} \tag{13}$$

Along stress paths activating plastic strains, such as water-undrained loading ($\dot{\boldsymbol{\sigma}} > 0, \dot{e_w} = 0$) or water volume injection at constant stress ($\dot{\boldsymbol{\sigma}} = 0, \dot{e_w} > 0$), the uniqueness and existence of the solution is no longer guaranteed when:

$$(H - H_w) \leq 0 \tag{14}$$

Such circumstance can occur also in hardening regime. In this case, hence, there is no direct correspondence between the onset of unstable processes and the softening regime. Moreover, the domain gathering unstable stress states (the so-called instability domain) is no readily apparent since it depends on soil properties and the evolving state of the material.

3. WR2-Unsat model

The stability criteria presented in a general form in the previous section can be specialized with reference to any constitutive model satisfying Eqs. (1)–(4). The model selected for this study is the WR2-Unsat model developed by Rotisciani et al. (2021) by extending to unsaturated conditions the formulation originally proposed by Boldini et al. (2019).

The WR2-Unsat model is a critical state-based hardening plasticity model aimed at reproducing the main features of the hydro-mechanical response of structured unsaturated soils under monotonic stress paths. The hierarchical model formulation permits to activate or exclude the various features of the model, depending on the specific kind of geomaterial to be modelled. Since the study here presented is restricted to unsaturated soils lacking of cementation bonds, the parts of the hardening law describing the destructuration phenomena are not considered in the following.

Here, the model formulation is summarised, specializing the constitutive functions to the class of material of interest. More details on the implications of the mechanical destructuring processes can be found in Rotisciani et al. (2021) and Boldini et al. (2019), the last one limited to the case of dry or fully saturated soils.

3.1. Constitutive laws

The WR2-Unsat is a single surface elasto-plastic model formulated in terms of Bishop's effective stress. The yield locus f delimiting the elastic domain is based on the expression proposed by Bigoni and Piccolroaz (2004), covering a wide range of frictional-cohesive materials:

$$f: \; -Np_c\sqrt{(\Phi - \Phi^{m})\left[2(1-\alpha)\Phi + \alpha\right]} + \frac{q}{h(\theta)} = 0 \tag{15}$$

where Φ is defined as: $\Phi = p'/p_c$; p' and q are the mean effective and deviatoric stress invariants; α ($0<\alpha<1$) and m ($m>1$) define the shape of the curve in the (q, p') plane whereas N ($N>0$) controls the pressure sensitivity; p_c is the hardening variable governing the current size of the yield locus. The function $h(\theta)$ expresses the dependence of f on the Lode angle θ and is defined as follows:

$$h(\theta) = \frac{1}{cos(\pi/3 - \beta\pi/6 - 1/3cos^{-1}(\gamma cos3\theta))} \tag{16}$$

Where γ ($0\leq\gamma<1$) and β ($0\leq\beta\leq2$) govern the shape of the yield locus in the deviatoric plane.

The plastic potential function g is expressed by a function similar to the one adopted for the yield locus:

$$g: \ -N_g p_{c,dummy}\sqrt{(\Phi_g - \Phi_g^{m_g})\left[2(1-\alpha_g)\Phi_g + \alpha_g\right]} + \frac{q}{h(\theta)} = 0 \tag{17}$$

where Φ_g is defined as: $p'/p_{c,dummy}$; $p_{c,dummy}$ has no physical meaning and only identifies the dimension of the g-locus passing through the current stress state; α_g, m_g, and N_g define the shape of the plastic potential in the (q, p') plane. Depending on the values of the shape parameters of f and g, the flow rule results as associated or not. In the deviatoric section, g always coincides with f.

Within the elastic domain, the reversible behaviour is described by the hyperelastic formulation which accounts for the non-linear dependency of the elastic stiffness on effective stress, originally proposed by Houlsby et al. (2005) and extended in Amorosi et al. (2020). The adopted free energy potential W has the following expression:

$$W = \frac{p_a}{2-n_e} k^{n_e/(2-2n_e)} (1-n_e)^{\frac{2-n_e}{1-n_e}} \left[k\left(\varepsilon_v^e\right)^2 + \frac{3g}{1-n}\left(\varepsilon_s^e\right)^2 \right]^{\frac{2-n_e}{2-2n_e}} \tag{18}$$

where ε_v^e and ε_s^e are the volumetric and deviatoric elastic strain invariants, p_a is a reference pressure corresponding to the atmospheric pressure, n_e, k, and g are dimensionless parameters to be determined experimentally.

The activation of plastic strains and/or any variation in saturation induce a homothetic evolution of the yield locus. The isotropic hardening law reads as follows:

$$\dot{p_c} = p_c\left[\frac{1}{\lambda^*}\dot{\varepsilon}_v^p - b\dot{S}_r\right] \tag{19}$$

where $\dot{\varepsilon}_v^p$ is the volumetric plastic strain rate, λ^* is the modified compression index evaluated in the bi-logarithmic compressibility plane and b is the coupling parameter controlling the hardening effects induced by the variations of the degree of saturation. The latter parameter has a clear geometrical meaning since it defines the relative position on the normal compression line (NCL) related to the current S_r with respect to the saturated one.

The non-hysteretic uncoupled retention behaviour is described by the well-known Van Genuchten Water Retention Curve (WRC):

$$S_r = S_{r,res} + \left(1 - S_{r,res}\right)/[1 + (\alpha_w s)^{n_w}]^{m_w} \tag{20}$$

where α_w is linked to the air-entry value, n_w and m_w control the shape of the curve and are related by the relationship: $m_w = 1 - 1/n_w$; $S_{r,res}$ is the residual saturation degree.

3.2. Stability criteria

The stability criteria expressed by Eqs. (8) and (14) are here specialized to the case of the WR2-Unsat model. In this model, the hardening variable controlling the dimension of the yield locus is p_c that, as mentioned above, evolves with the volumetric plastic strains and the degree of saturation.

In net stress and suction-controlled loading tests, thus, the soil response is no longer defined when:

$$H = -\frac{\partial f}{\partial p_c}\frac{p_c}{\lambda^*}\frac{\partial g}{\partial p'} \leq 0 \tag{21}$$

On the wet side, $\partial g/\partial p' \geq 0$, the unique incremental solution can always be computed. The potential instability domain coincides with the dry side of the yield surface, where the soil exhibits a strain-softening response.

Under loading paths imposed controlling net stress and water flux, the potential instability occurs when Eq. (14) is satisfied. Considering the constitutive assumptions of the WR2-Unsat model, Eq. (14) can be rewritten in the following form (see Appendix C):

$$-\frac{\partial f}{\partial p_c}\frac{p_c}{\lambda^*}\frac{\partial g}{\partial p'} - \frac{\left[\frac{\partial f}{\partial p'}\left(s + \frac{\partial s}{\partial S_r}S_r\right) - \frac{\partial f}{\partial p_c}bp_c\right]}{\left[1 - \frac{1}{K}\frac{S_r}{n}\left(s + \frac{\partial s}{\partial S_r}S_r\right)\right]}\frac{\partial g}{\partial p'}\frac{S_r}{n} \leq 0 \tag{22}$$

Being K the elastic bulk modulus.

On the wet side, the previous expression can be rearranged as follows:

$$\left[\left(-\frac{\partial f}{\partial p'}\Big/\frac{\partial f}{\partial p_c}\frac{\lambda^*}{p_c} + \frac{1}{K}\right)\left(s + \frac{\partial s}{\partial S_r}S_r\right) + b\lambda^*\right]\frac{S_r}{n} \geq 1 \tag{23}$$

By placing:

$$n_{lim} = \left[\left(-\frac{\partial f}{\partial p'}\Big/\frac{\partial f}{\partial p_c}\frac{\lambda^*}{p_c} + \frac{1}{K}\right)\left(s + \frac{\partial s}{\partial S_r}S_r\right) + b\lambda^*\right]S_r \tag{24}$$

Eq. (23) can be simplified into:

$$n \leq n_{lim} \tag{25}$$

According to Eq. (25), the uniqueness of the incremental response under a water-undrained loading path or an imbibition process at constant net stress is no longer guaranteed when the porosity becomes lower than n_{lim}. The latter defines the porosity below which the hydro-mechanical coupling becomes critical, causing the triggering of an instability mechanism before attaining critical state conditions.

Eq. (25) suggests an important difference between this case and the previous one. Under water content-controlled conditions, it is impossible to define a priori an instability domain: any stress path is potentially unstable, even the isotropic one. The activation of the instability depends on the material state and its evolution under the imposed loading process rather than on the specific stress path followed.

Moreover, the control of water content involves a strong coupling between the hydraulic and mechanical response that can cause the onset of unstable conditions also in the hardening regime ($H>0$). Under a given perturbation, the changes in suction and saturation degree modify the effective stress distribution causing soil deformations that, in turn, affect the values of suction and saturation degree. This process can lead to an unstable response resulting from an uncontrolled growth of the pore water pressures and soil deformations.

The proposed criterion highlights all the variables that influence soil stability. It should be noted that some of them are parameters, i.e. do not vary during any process (b, λ^*, the shape of WRC), while others can evolve along a generic stress path (p', η, p_c, s, S_r). The influence of the latter variables is thus highly dependent on the specific case under consideration. This paper evaluates their relevance with reference to the case of shallow unsaturated slopes exposed to rainfall events.

4. Material stability during water infiltration

The stability criteria presented in the previous section are here used to capture the initiation of uncontrolled deformation processes during

water infiltration. Such processes can cause the triggering of static liquefaction and, thus, the evolution of slope failure into flowslides. The main purpose of this first part of the study is to provide a consistent explanation of the above processes by i) clarifying their causes; ii) modelling their activation; and iii) defining the impact of boundary conditions on the stability scenarios.

The investigation refers to the case of an ideal infinite slope subjected to rainfall events. The slope is composed by a shallow layer resting on a rigid bedrock inclined at 30° to the horizontal. The unsaturated shallow cover consists of a lightly over-consolidated coarse-grained soil with low plasticity fine. Its hydro-mechanical soil behaviour was modelled by combining the WR2-unsat model and the Van Genuchten water retention model, as discussed in § 4.1.

The numerical study was conducted using the finite element code Abaqus/Standard, where the WR2-unsat model was implemented adopting an explicit Euler scheme with error control (Boldini at al., 2019, Rotisciani et al., 2021). The study was developed in two steps. The first one is devoted to the analysis of the geostatic stress distribution within the infinite slope (§ 4.2), while the second inspects the effects of water infiltration with reference to a soil element located at the base of the shallow cover (§ 4.3). This portion of the shallow deposit is the most critical for the triggering of landslides, especially when rains are light and prolonged in time. Therefore, the numerical simulations of the wetting process are essentially material point-level analyses and aim to identify the conditions under which wetting instabilities become possible.

4.1. Model calibration

The set of hydro-mechanical parameters used in the numerical simulations is listed in Table 1. The model was calibrated with reference to typical data reported in the literature for coarse grained soils with non plastic silty fraction, which represent the class of materials most commonly involved in flowslides.

The distorted shape of the elastic domain (α=0, $m = 2$, N=1.1) in the (q,p') plane stems from the results of undrained compression triaxial tests carried out on real non-plastic materials including sand and sandy silt (Zlatović and Ishihara, 1997; Zlatović and Ishihara, 1998). The yield locus shown in Fig. 1a is characterized by a stress ratio at the maximum deviatoric stress η_p equal to 0.9 and a dry side flattened on the critical state line (CSL), this latter being characterised by a slope N_g equal to 1.33. For the sake of simplicity, the yield surface is assumed to be independent of the Lode angle ($\beta = 1$, $\gamma = 0$). In the deviatoric section, thus, the yield surface degenerates into a circle.

The plastic potential function coincides to the ellipse of the Modified Cam Clay model ($\alpha_g = 0$, $m_g = 2$, $N_g = 1.33$). Therefore, the material exhibits a contractive behaviour along all the stress–strain paths attaining yielding at stress ratios lower than N_g.

The dimensionless shear stiffness parameter that controls the soil response in the elastic domain was determined according to the expressions available in literature for coarse-grained soils (Hardin and Black, 1966; Seed et al., 1986; Lo Presti, 1989), assuming for n_e and p_a the values of 0.5 and 1 kPa, respectively. The dimensionless bulk modulus k was derived from the corresponding shear one, g, assuming a Poisson's ratio equal to 0.25 under isotropic stress conditions.

The position and the slope of the NCL of the adopted ideal material was selected based on available data for sands, silty sands, and sandy silts (Olson and Stark, 2003; Olson and Mattson, 2008; Jefferies and Been, 2015). The hydro-mechanical coupling term was determined according to the data reported in Gallipoli et al. (2003, 2008), Wong et al. (2014), Rotisciani et al. (2014), Catteneo et al. (2014). The experimental data reveal a large variation range for both hardening parameters: 0.01—0.05 for λ^*, 1–5 for b. The values adopted in the analysis are intended to emphasize the potential for wetting collapse.

Finally, the parameters controlling the retention behavior derive from the analysis of a large set of experimental data related to sands and silty sands (Benson et al., 2014; Gallage and Uchimura, 2010; Likos and Godt, 2014; Nicotera et al., 2015). The WRC adopted in this study is characterized by a low air-entry value and a residual degree of saturation close to zero (Fig. 1b).

4.2. Phase 1: geostatic conditions

The infinite slope considered in this study consists of a shallow unsaturated soil layer 1.2 m thick covering a bedrock inclined at 30° to the horizontal (Fig. 2a). Given the initial overconsolidated state, throughout the geostatic initialization stage the soil behaves as a hyperelastic material. At this stage, pore water pressure is uniformly distributed within the soil layer and equal to about −10 kPa. The degree of saturation S_{r0} resulting from the WRC is 0.76. The total vertical stresses increase with depth with a gradient of 19 kN/m^3. The vertical effective stress σ_z' varies linearly with depth, assuming at the soil surface a value corresponding to the product between suction and saturation degree, consistently with the Bishop's effective stress definition (Fig. 2b). Horizontal effective σ_x' and shear τ_{xz} stresses also increase linearly with depth, though with smaller gradients. The stress ratio η exhibits a nonlinear variation with depth and reaches a value of 0.8 at the base of the soil layer (Fig. 2c).

4.3. Phase 2: effects of water infiltration on soil response

The effects of water infiltration on soil response were inspected by restricting the numerical analyses to a single soil element located at the base of the shallow cover of the idealised slope under study (at a depth z_b equal to 1.1 m).

The wetting tests presented in this section were conducted on a single eight-node element under axial-symmetric loading conditions by keeping constant the applied total stresses. Those conditions do not coincide with the plane strains ones imposed in the previous geostatic stage, while being consistent with those adopted in §3.2 where the stability indexes were derived. This modelling choice was suggested by the results of preliminary analyses, which confirmed the good match between wetting-induced soil responses under axisymmetric and plane strain conditions, provided that the yield locus is independent of the Lode angle, as assumed here. Another evidence emerging from the preliminary analyses was that the out-of-plane net stress experiences small changes during wetting, again confirming the validity of the hypothesis of axisymmetric analysis conditions here assumed.

The wetting processes were modelled using two strategies: i) by reducing the suction level at a constant rate (Test 0); ii) by imposing a water inflow of constant intensity (Test 1). The first scenario reproduces the boundary conditions imposed in geotechnical laboratory experiments aimed at investigating the soil response during wetting (see

Table 1
Constitutive parameters.

Elastic parameters		Yield surface parameters		Plastic potential function parameters		Hardening parameters		Water retention curve parameters	
n_e	0.5	α	0	α_g	1.0	λ^*	0.05	α_w	0.201 kPa^{-1}
p_a	1 kPa	m	2.0	m_g	2.0	b	5	m_w	0.2338
k	6666.7	N	1.1	N_g	1.33			n_w	1.305
g	5000	β	1					$S_{r,res}$	0.073
		γ	0						

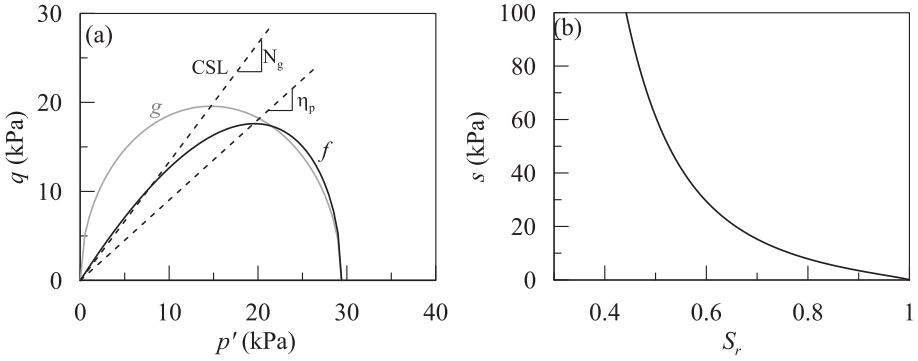

Fig. 1. a) yield surface and plastic potential function; b) water retention curve.

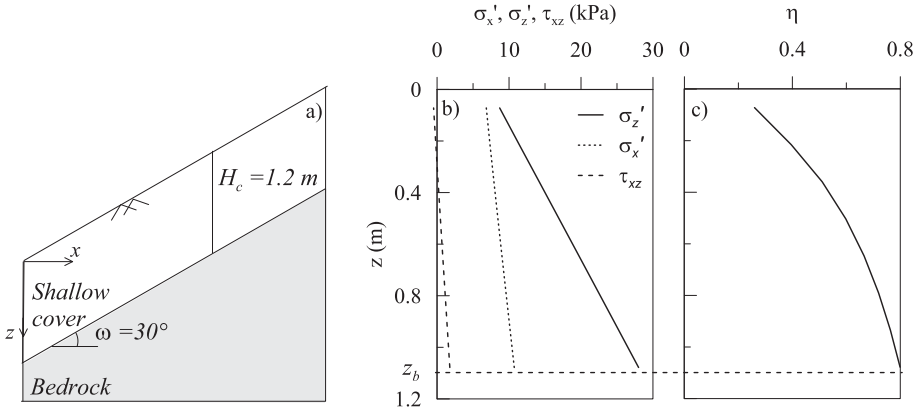

Fig. 2. a) geometry of the ideal infinite slope; b) profiles with depth of effective horizontal, vertical and shear stresses; c) profile with depth of stress ratio.

Olivares and Damiano, 2007, Cuomo et al., 2017). The second mimics the boundary conditions expected in unsaturated slopes during rainfall events, although they are not exactly the same. In situ, the intensity of water inflow is likely to vary with time, according to the temporal variation of rainfall intensity and the evolving state of the material, and with depth. The variation in water content is therefore unknown a priori, but the imbibition process at the local level is certainly due to a water inflow. Consequently, wetting tests performed by imposing a water inflow should give a more realistic picture of the in situ response than standard wetting tests where suction is controlled. However, experimental evidence for these non-standard tests is not yet available because of the difficulties in performing them in the laboratory. Indeed, the standard devices should be modified to allow the water content to be controlled by injecting a constant water flow while keeping the net stresses unchanged.

The initial conditions, soil properties and boundary conditions for the wetting tests are summarized in Table 2. The initial stress state stems from the preliminary analyses conducted on the infinite slope under geostatic conditions. Consistently with the selected modelling approach, the initial stress state was slightly modified by assuming a zero Lode angle. The material is lightly over-consolidated with an over-consolidation ratio R of 1.1, where R is defined as ratio between p_c and the intersection with the p' axis of the yield locus passing through the initial stress state. Given the low compressibility in the elastic domain, the initial specific volume v_0 coincides with that corresponding to p_c on the NCL for the assumed initial degree of saturation S_{r0} (Rotisciani et al., 2020). Tests 0 and 1 differ only in the imposed boundary conditions.

Consider now suction-controlled Test 0. Fig. 3 shows a 3D representation of the wetting-induced stress path. The loss of suction entails a gradual reduction in mean effective stress under constant deviatoric stress (path AF). The current stress ratio increases, never exceeding N_g. Despite the stress unloading, the initial homothetic contraction of the yield surface due to the increase in S_r is such to intercept the current stress state and maintains it in the elasto-plastic regime. Upon exceeding the stress ratio η_p, the yield locus starts to increase in size following the stress state. This response results from the development of positive plastic volumetric strains that counterbalance the softening induced by S_r changes.

Fig. 4 shows a) the evolution of both saturation degree and volumetric strains with pore water pressures, b) the evolution of hardening modulus and water ratio with pore water pressures. The reduction in suction causes the onset of volumetric collapse resulting in a contractive soil behavior (Fig. 4a). Assuming an uncoupled retention response, the changes in the degree of saturation follow the ones imposed on the suction. The simulation ends upon reaching full saturation. The attainment of final stationary values of ε_v and S_r proves the stability of the soil response. The uniqueness and existence of the solution are further

Table 2
Initial conditions and soil properties adopted in the numerical simulations.

Test	p_0'(kPa)	q_0 (kPa)	η_0	s_0 (kPa)	S_{r0}	p_{c0} (kPa)	v_0	b	λ	CV
0	19.66	15.9	0.8	10.0	0.765	29.4	1.79	5	0.05	$\dot{u}_w$
1	19.66	15.9	0.8	10.0	0.765	29.4	1.79	5	0.05	$\dot{e}_w$

CV: stands for Control Variable.

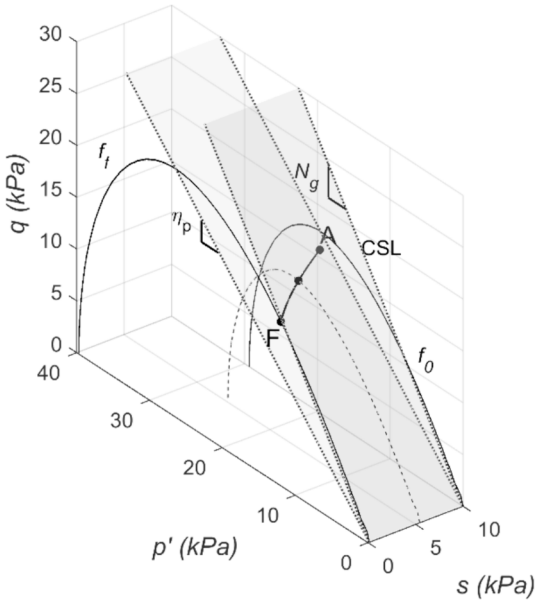

Fig. 3. Stress path followed in Test 0.

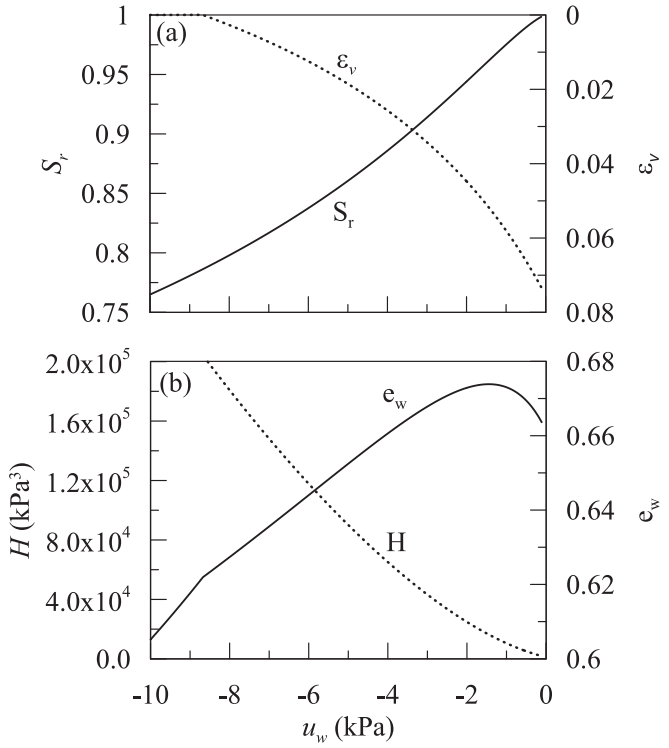

Fig. 4. Results of Test 0: a) evolution of degree of saturation and volumetric strains, b) evolution of hardening modulus and water ratio during wetting.

confirmed by the positive values of the hardening modulus H that exclude the onset of a drained shear failure (Fig. 4b). The latter is the only instability mechanism that can take place under the imposed boundary conditions. During the wetting process, the water ratio e_w increases up to a peak value and then slightly decreases (Fig. 4b). The final reduction in water volume stems from the combined effect of the volumetric collapse of the solid skeleton and the imposed variation of the degree of saturation. In other words, when fully saturation conditions are approached, the fulfilment of the constraint on S_r in a collapsible soil sample, as the one considered in this test, forces the water to flow out from the soil element. This result suggests a latent instability that can be activated switching from suction-controlled to water content-controlled test, as confirmed by the results of the Test 1.

Test 1 differs from the previous one only for the imposed boundary conditions (see Table 2). The injection of water volume entails a reduction in suction and consequent stress unloading at constant deviatoric stress, similarly to what observed in Test 0 (path AF in Fig. 5). The pore water pressure exhibits an abrupt increase upon exceeding −3 kPa (Fig. 6). At the same time, the rate of volumetric strains starts to increase steadily, highlighting the inability of the soil to further sustain the applied loading. The onset of the volumetric instability causes the immediate end of the simulation, preventing the attainment of full saturation. This instability develops with an uncontrolled growth of the pore water pressures and continuous changes in soil particle configuration. Such mechanism is similar to the one activating static liquefaction in fully saturated soils. Both unstable phenomena are diffuse instabilities, occur in the hardening regime, i.e. before classical shear failure, and are due to the strong interplay between mechanical and hydraulic variables that mutually interact leading to the loss of control of soil response.

It is important to note that the simulation ends at the same suction level observed in Test 0 after reaching the maximum water ratio. Moreover, the volumetric instability occurs when the current stress ratio is in the range 0.89–1.33, corresponding to the undrained instability domain. The latter circumstance reveals the possibility of two successive instability mechanisms leading to the evolution of landslides in flowslides. A first instability might occur before full saturation is attained, as in the above simulation, then followed by further catastrophic evolution towards static liquefaction upon attainment of saturation. What above provides a new perspective in the interpretation of the complex triggering of real flowslides that occurred in the past (e.g., in the Campania region at the foothills of Mt. Pizzo d'Alvano mountain (Pirone et al. 2015) or in Mount Cornito hillslope (Comegna et al., 2016)) though here only developed with reference to an idealised, yet realistic, case.

The instability conditions emerging in this simulation can be predicted by monitoring the stability index derived in §3.2. In detail, under the imposed boundary conditions, the initiation of instability can be captured by monitoring separately the evolution of n_{lim} and n during wetting (Fig. 7a). The porosity is initially greater than the threshold value, consistently with the initially stable response of the soil. The injection of water volume causes *i*) a small reduction in soil porosity

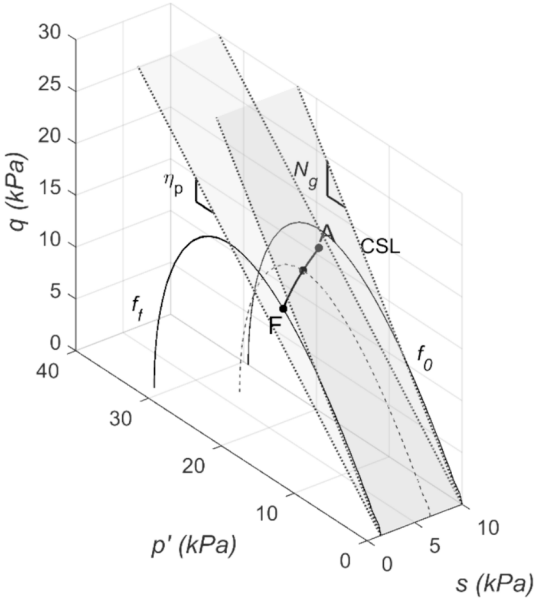

Fig. 5. Stress path followed in Test 1.

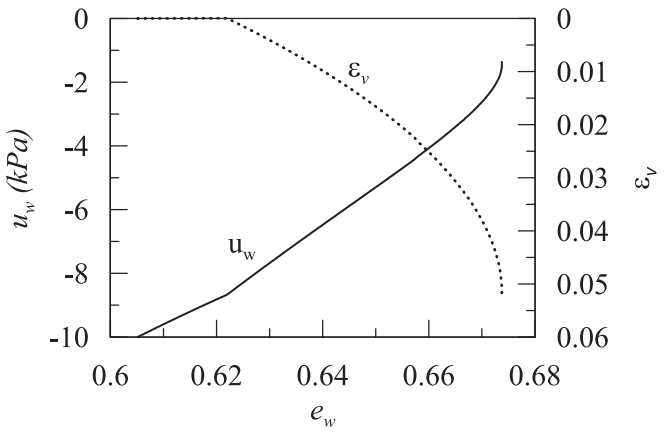

Fig. 6. Evolution of degree of saturation and volumetric strains during wetting in Test 1.

resulting from the collapse of the solid skeleton; *ii*) a significant increase in n_{lim}. Initially, n_{lim} varies almost linearly with S_r, with a slope mainly depending on the b and λ^* values. In the first phase, the small suction level and the low slope of the WRC make the first term in Eq. (24) barely relevant. When approaching full saturation, the curve (n_{lim}, S_r) exhibits a marked increase resulting from the significant reduction in the slope of the WRC. Consequently, the n_{lim} values appreciably increase making the onset of an instability mechanism highly probable. The simulation ends when n equals n_{lim}. The latter circumstance corresponds to the occurrence of the abovementioned instability mode that gives rise to uncontrolled growth of pore pressures and soil deformations.

Alternatively, soil stability can be checked by monitoring the evolution of the difference between n_{lim} and n, normalized with respect to the initial porosity n_0, $(n-n_{lim})/n_0$ (Fig. 7b). Besides making readily apparent the onset of instability, the use of this variable is convenient since: i) it combines the effects of the two variables affecting soil stability, ii) simplifies the graphical representation of the numerical results, and iii) facilitates the comparison between the results related to different tests. It is worth noting that because of the small variations of n, the changes in $(n-n_{lim})/n_0$ reflect the ones observed for the threshold value.

In conclusion, the results of the numerical simulations demonstrate that the volumetric instability occurring under water content controlled conditions can be captured by monitoring:

i) the variable $(n-n_{lim})/n_0$, which acts as a sort of compact descriptor of the current stability conditions. Its positive values indicate stable conditions, while zero values point out the occurrence of actual or potential instabilities, depending on the set of the imposed state variables. In slope stability analyses, this variable can help to interpret a-posteriori the soil response during rainfall events, by promptly pointing out the triggering of an unstable process at the local level. However, the large number of variables on which it depends prevents its inclusion or adoption in early warning systems.

ii) the evolution of e_w. Such a variable can be measured indirectly using the data provided by the monitoring systems commonly installed in situ (e_w is a function of S_r and e) without additional costs related to the installation of new devices. Taking into account the strong correlation between $(n-n_{lim})/n_0$ and $\dot{e}_w$ (the former vanishes when the second attains its maximum value), the analysis of the gathered data should focus on the global trend of the curves (S_r, e_w) or (u_w, e_w). Particular attention should be paid to any reduction in slope, which could indicate a potential loss of slope stability.

5. Influence of soil properties and slope geometry on soil stability

Here we aim at generalizing the outcomes of the previous section, exploring the influence of soil properties and slope geometry on the stability of a soil element at the base of a shallow slope deposit. This is achieved by parametrically modifying the key parameters prior to numerically subjecting the soil element to a costant rate water inflow under constant net stresses, i.e. the conditions adopted in Test 1 of the previous section. The range explored for each of the parameters was defined based on those characterizing real slopes involved in rainfall-induced flowslides. The final objective of the analyses is to identify the most critical scenarios for slope stability, providing a guideline to recognize slopes prone to instability, for which detailed coupled hydro-mechanical stability analyses are recommended.

As previously discussed, the imposed water inflow boundary conditions activate instability, reproducing locally what occurs globally in real slopes; it allows the identification of the exact moment when such a phenomenon occurs, which coincides with the attainment of the volumetric instability in the soil.

The main characteristics of the tests are listed in Table 3. Tests from 1 to 7 inspect the influence on slope stability of the material properties, while those from 8 to 11 focus on the role of the slope geometry. In the first series of tests, the range of variation of each parameter (b, λ, WRC) covers the one typically observed for coarse-grained soil with non-plastic fine. Tests 8 to 11 correspond to slope angle ω ranging from 20° in Tests 8 to 38° in Test 9 whereas the thickness of the shallow deposit H_c goes from 0.5 m in Test 10 to 2 m in Test 11.

5.1. Influence of soil properties

Tests 1, 2, and 3 investigate the influence of b, the parameter controlling the hydro-mechanical coupling on the soil response. While modifying the interaction between hydraulic and mechanical variables, the increase of the b-value entails an increase in v_0 resulting from the increasing distance between the saturated NCL and the one related to S_{r0}. In all the tests, the response becomes unstable before attaining full saturation. The triggering of the volumetric instability causes the

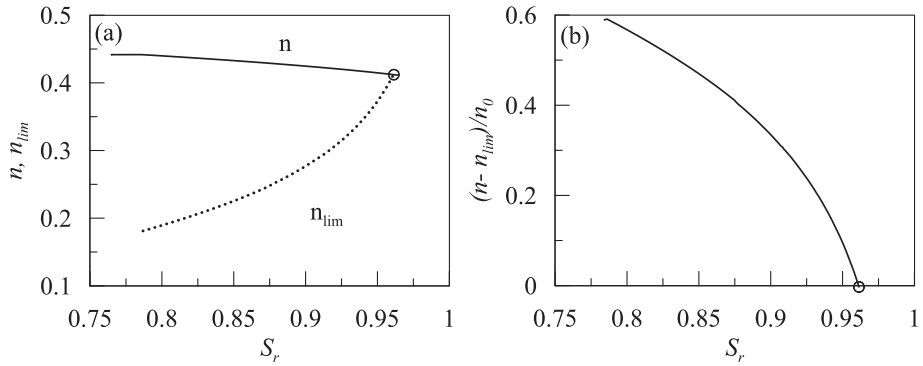

Fig. 7. Test 1: evolution of a) n and n_{lim}; b) $(n-n_{lim})/n_0$ during wetting.

Table 3
Slope geometry, initial conditions and soil properties adopted in the parametric study (Bold identifies the reference analysis).

Test	p_0' (kPa)	q_0 (kPa)	η_0	s_0 (kPa)	S_{r0}	p_{c0} (kPa)	v_0	b	λ^*	ω (°)	H_C (m)
1	**19.66**	**15.9**	**0.8**	**10.0**	**0.765**	**29.4**	**1.79**	**5**	**0.05**	**30**	**1.0**
2	19.66	15.9	0.8	10.0	0.765	29.4	1.75	3	0.05	30	1.0
3	19.66	15.9	0.8	10.0	0.765	29.4	1.72	1.5	0.05	30	1.0
4	19.66	15.9	0.8	10.0	0.765	29.4	1.87	5	0.03	30	1.0
5	19.66	15.9	0.8	10.0	0.765	29.4	1.95	5	0.01	30	1.0
6	15.92	12.74	0.8	2.5	0.765	23.82	1.81	5	0.05	30	1.0
7	47.19	37.75	0.8	65.1	0.765	70.57	1.71	5	0.05	30	1.0
8	20.70	13.52	0.65	10.0	0.765	26.32	1.80	5	0.05	20	1.0
9	17.06	16.67	0.97	10.0	0.765	32.63	1.78	5	0.05	38	1.0
10	12.45	7.51	0.6	10.0	0.765	16.12	1.84	5	0.05	30	0.5
11	29.81	29.36	0.98	10.0	0.765	54.74	1.73	5	0.05	30	2.0

immediate stop of the numerical simulation. The injection of water volume entails a progressive reduction of the mean effective stress, keeping unaltered the deviatoric stress component (Fig. 8a), thus leading to an increase of the stress ratio, though never exceeding the critical state one. This circumstance excludes the possibility that the instability results from a more conventional drained shear failure. It is worth noting that, irrespectively of the value of b, the volumetric instability takes place within the potential liquefaction domain (grey region in Fig. 8a). Such an evidence suggests the possibility of a subsequent instability upon attaining full saturation, leading to the triggering of static liquefaction.

Fig. 8b shows the evolution of $(n-n_{lim})/n_0$ during wetting. In all the three cases, $(n-n_{lim})/n_0$ decreases with increasing saturation levels, vanishing before the complete removal of suction. This result confirms the triggering of the volumetric instability characterized by an uncontrolled growth of soil deformations and pore water pressures. Increasing the value of b intensifies the hydro-mechanical coupling, enhancing instability. This tendency is confirmed by the reduction in the initial value of $(n-n_{lim})/n_0$ and its increasingly rapid decrease with S_r as b increases.

Tests 1, 4, and 5 explore the impact of compressibility λ^* on soil stability. The reduction of λ^* entails an increase in the specific volume corresponding to the initial stress state, this latter being kept unaltered in the three tests. The results shown in Fig. 9a share several features with the ones depicted in Fig. 8a. The stress paths move horizontally towards decreasing mean effective stresses. The final stress states lie below the CSL within the potential liquefaction domain.

Fig. 9b, illustrating the evolution of $(n-n_{lim})/n_0$ with S_r, reveals the marked influence of λ^* on soil stability. In low compressible soils, the response remains stable even after the complete removal of suction (see Test 5 for example). For higher values of λ^* the response becomes unstable before attaining full saturation. In such circumstance, increasing compressibility leads to a loss of control taking place under decreasing degrees of saturation. As already noticed with reference to parameter b, high λ^*values facilitate wetting collapse, enhancing the coupling between mechanical and hydraulic variables. Such a tendency increases the chances of occurrence of unstable phenomena, as confirmed by the reduction in the initial distance between n and n_{lim} and the rapid vanishing of their difference.

Tests 1, 6, and 7 investigate the influence of the retention behaviour on the soil response. The WRCs employed in the numerical analyses are representative of the retention behaviour of coarse-grained soils with different fine fractions (Fig. 10). Materials lacking of fine fraction present sub-horizontal WRCs with very low air entry values (see WRC_6 in Fig. 10). In materials with non-negligible fine fractions, the shape of the WRC depends on soil grading: increasing fine fraction involves increasing air-entry values, controlled in the Van Genuchten model by the parameter a_w, and increasing slope of the curve, defined by parameter n_w (see WRC_7 in Fig. 10). Such changes entail a variation in the suction level corresponding to the initial degree of saturation that, in turn, reflects on the initial values of all state variables. In detail, going from Test 6 to Test 7, stress invariants and p_{c0} increase whereas the specific volume decreases.

Even in these cases the stress paths move horizontally towards decreasing mean effective stresses (Fig. 11a). All final stress states lie within the potential liquefaction domain. The results depicted in Fig. 11b reveal that the soil response remains stable only in Test 6. In this case, the current porosity keeps greater than the threshold value even when full saturation is approached. In this test, despite the contractive soil behaviour, the combined effect of high porosity, low slope of the

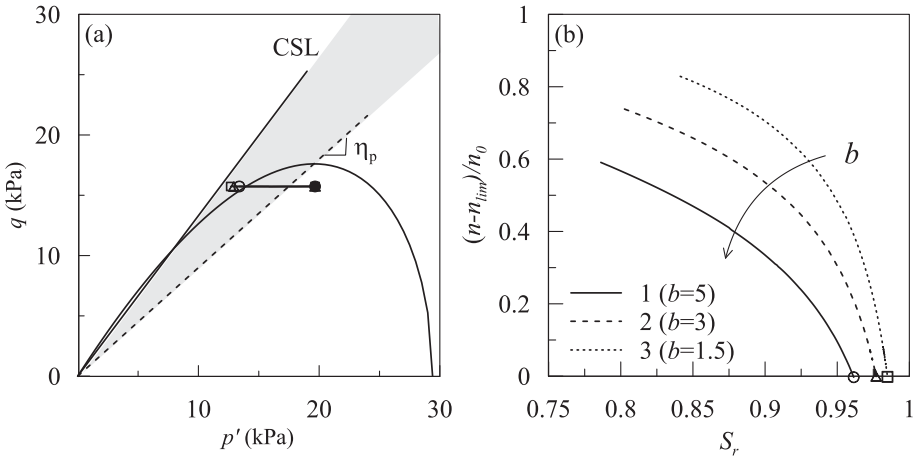

Fig. 8. Influence of the b-value on soil stability: a) wetting-induced stress path (full symbols: Initial conditions; empty symbols: final conditions); b) evolution of $(n-n_{lim})/n_0$ with S_r.

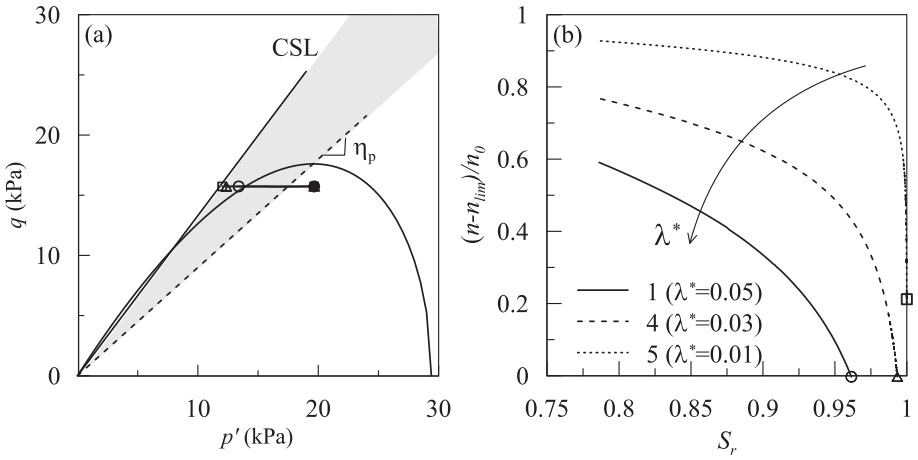

Fig. 9. Influence of the λ^*-value on soil stability: a) wetting-induced stress path (full symbols: Initial conditions; empty symbols: final conditions); b) evolution of $(n-n_{lim})/n_0$ with S_r.

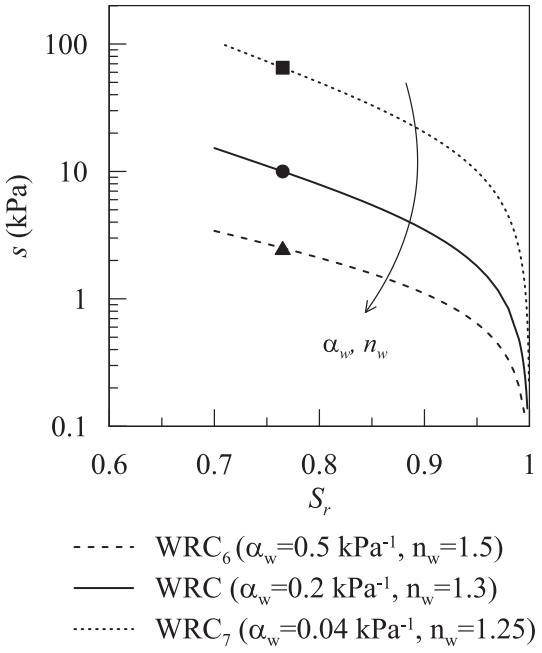

Fig. 10. WRCs adopted in the numerical simulations.

WRC, and small suction levels limits the hydro-mechanical coupling making the triggering of the volumetric instability unlikely. In the other two cases, n equals n_{lim} before the complete removal of suction. The transition from a stable to unstable response occurs under saturation levels that decrease as the a_w- and n_w-values decrease. Such a result highlights that critical conditions may occur when intense rainfalls involve deposits consisting of coarse-grained soils with non-negligible fine fractions.

In summary, the results shown in this subsection reveal that the most critical scenarios for slope stability are those involving:

- materials characterized by high b or λ^*values. Such materials experience a volume compaction upon saturation, sufficient to trigger an uncontrolled saturation that can lead to a subsequent undrained instability in soils susceptible to liquefaction;
- coarse-grained soils with non-negligible fine fractions. The presence of fine materials i) enhances the tendency to collapse, favouring instability in the unsaturated regime; ii) reduces soil permeability, allowing positive excess pore water pressures to be retained until the final occurrence of instability in the fully saturated regime.

5.2. Influence of slope geometry

Tests 3, 8, and 9 explore the influence of the slope angle ω on soil stability. The increase in ω from 20° to 38° entails an increase in the stress ratio η_0 due to the increase in the deviatoric component and a reduction in the isotropic one (see Table 3). The changes in the initial effective stress state also involve variations in the initial

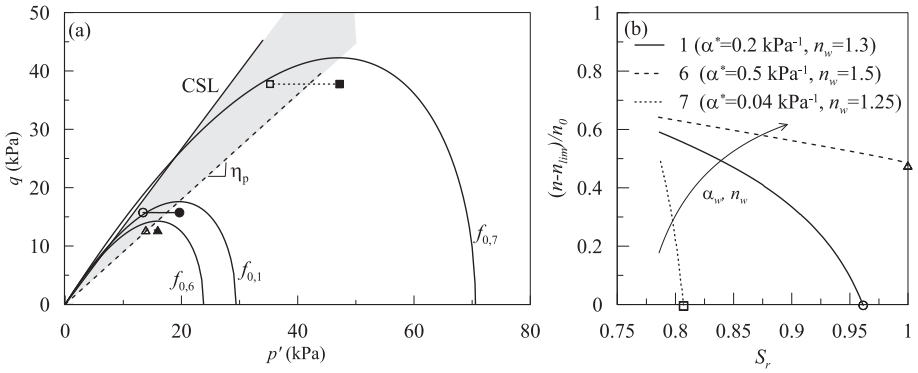

Fig. 11. Influence of the WRC on soil stability: a) wetting-induced stress path (full symbols: Initial conditions; empty symbols: final conditions); b) evolution of $(n-n_{lim})/n_0$ with S_r.

preconsolidation pressure (p_{c0} increases) and specific volume (v_0 decreases).

Fig. 12a shows the wetting-induced stress path and the initial yield locus for each test. In all the three cases, the stress path moves horizontally and ends before attaining the classical shear failure. The final stress ratio differs in the tests but in all cases is greater than η_p.

Starting from low stress ratios (gentle slopes), the soil response remains stable during the injection of water volume (Fig. 12b). In fact, the soil attains fully saturated conditions for positive values of $(n-n_{lim})/n_0$. On the contrary, for relatively steep slopes, characterised by high stress ratios, the sample already exhibits an unstable response in the unsaturated regime. The instability reveals the inability of the soil to withstand the applied loadings and takes place at decreasing degrees of saturation for increasing η_0. Correspondingly, the numerical results highlight a marked influence of η_0 on the position and shape of the $(n-n_{lim})/n_0$-curve. More specifically, the curve shifts downwards and its slope increases decreases as η_0 increases. This trend indicates that the risks associated with the onset of instability mechanisms increase significantly at high stress ratios (steep slopes), where small changes in S_r and n are sufficient to trigger the instability. These results confirm the marked influence of the initial stress ratio on the wetting-induced soil response, as already observed experimentally in several laboratory tests under triaxial and simple shear conditions (Olivares and Damiano, 2007: Cuomo et al., 2017).

Finally, Tests 1, 10 and 11 explore the influence of the thickness H_c of the shallow soil deposit on the overall soil stability, with H_c equal to 1.0, 0.5 and 2 m respectively. The suction level was kept unaltered in all the three tests and, as in the other cases, the simulations were carried out with reference to an element located at the base of the soil deposit. Besides affecting the single stress components, any change in the H_c influences the ratio between the two stress invariants. As the thickness of the shallow cover decreases, its weight decreases and so does the initial stress ratio, the value of which is increasingly influenced by the product of suction and degree of saturation. As a side effect, the reduction of the stress state entails a reduction of p_c and an increase in the specific volume.

Fig. 13a shows the stress paths followed by the three elements and the initial yield locus for each test. In all three cases, the material is initially overconsolidated and experiences a reduction in the mean effective stress under constant deviatoric stress upon wetting. The final stress state lies on the portion of the yield locus included between η_p and N_g.

Regardless of the value of H_c, the simulation ends before attaining full saturation. The transition from stable to unstable conditions is pointed by the vanishing of the difference between the current and threshold porosities (Fig. 13b). Despite the beneficial effect of the reduction in η_0, the instability occurs before in Test 10 than in the other tests. This evidence proves that the increase in stress state due to the deepening of the shallow cover improves soil stability, limiting the wetting-induced volumetric collapses and the resulting changes in pore water pressures. In brief, i) the risk of instability is surely higher at shallow depths, ii) the most critical scenario is not known a priori since it results from the combination of the two competing factors η_0 and H_c.

6. Concluding remarks

This study aims at providing a novel explanation for the triggering of landslides in partially saturated coarse-grained soils evolving into flowslides, emphasising that such phenomena may result from the combination of two successive instabilities. The first occurs when the soil is still in the unsaturated regime and develops through uncontrolled build-up of pore water pressures and continuous evolution of the soil skeleton configuration. This instability can then catastrophically evolve into static liquefaction upon the attainment of full saturation.

This work focuses on the first instability occurring in the unsaturated regime and proposes an analytical criterion to capture the onset of wetting instabilities. The criterion is first derived theoretically in a general form and then specialised to a recently proposed constitutive model for fully and partially saturated soils, which also takes into account the effect of bond degradation. Finally, the criterion is used to monitor the stability of an ideal infinite slope consisting of a shallow unsaturated cover resting on a rigid bedrock during rainfall events. The effects of water infiltration are assessed by focusing on an elementary soil volume located at the base of the unsaturated cover. This portion of the shallow deposit is the most critical for the triggering of landslides, especially when rains are light and prolonged in time. The numerical results shown in the previous sections reveal that:

- unstable deformation patterns can take place during wetting processes when the soil is still in the unsaturated regime;
- the occurrence of these instabilities depends on the imposed boundary conditions: the control is lost only in water content-controlled tests. Such a scenario mimics the actual boundary conditions occurring in unsaturated shallow slopes during rainfall events;
- the volumetric instability is due to the strong interplay between mechanical and hydraulic variables that mutually interact leading to uncontrolled increases in pore water pressures, pore saturation, and soil deformation. This mechanism shares several aspects with the one controlling static liquefaction in fully saturated soils;
- the variable $(n-n_{lim})/n_0$ captures the initiation of unstable deformation processes during wetting and, thus, results in a suitable index

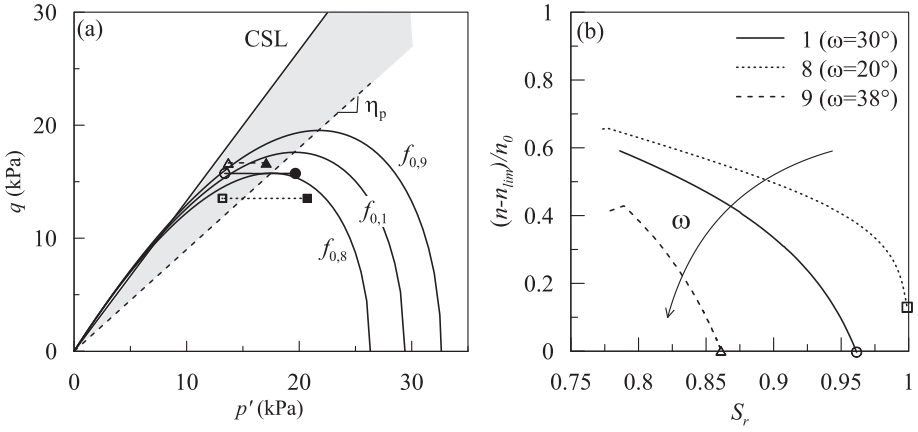

Fig. 12. Influence of the slope angle on soil stability: a) wetting-induced stress path (full symbols: Initial conditions; empty symbols: final conditions); b) evolution of $(n-n_{lim})/n_0$ with S_r.

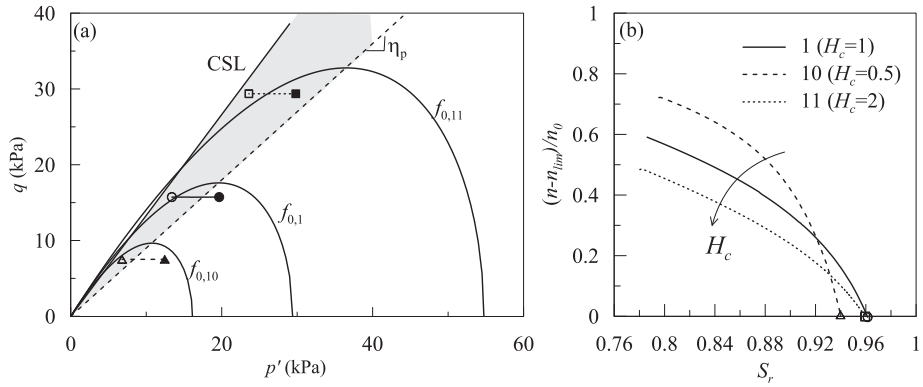

Fig. 13. Influence of the thickness of the shallow cover on soil stability: a) wetting-induced stress path (full symbols: Initial conditions; empty symbols: final conditions); b) evolution of $(n-n_{lim})/n_0$ with S_r.

for interpreting the response of shallow unsaturated slopes at the local level;
- The strict correlation linking $(n-n_{lim})/n_0$ and $\dot{e}_w$ suggests the use of the latter variable to monitor in real time the local stability of shallow unsaturated covers;
- the most critical scenarios for slope stability are those involving i) relatively steep slopes; ii) materials susceptible to liquefaction; iii) highly collapsible and/or compressive coarse-grained soils with low fine fractions; iv) shallow covers, with thickness lower than a couple of meters.

CRediT authorship contribution statement

G.M. Rotisciani: Writing – original draft, Methodology, Formal analysis, Conceptualization. **F. Novelli:** Software, Formal analysis. **A. Desideri:** Writing – review & editing, Supervision, Methodology, Funding acquisition, Conceptualization. **A. Amorosi:** Writing – original draft, Supervision, Methodology, Funding acquisition, Conceptualization.

Declaration of competing interest

The authors declare that they have no known competing financial interests or personal relationships that could have appeared to influence the work reported in this paper.

Data availability

No data was used for the research described in the article.

Acknowledgements

The authors acknowledge the support by the research project RETURN - multi-Risk sciEnce for resilienT commUnities undeR a changiNg climate - funded by the European Union Next-GenerationEU (National Recovery and Resilience Plan – NRRP, Mission 4, Component 2, Investment 1.3 – D.D. 1243 2/8/2022, PE0000005).

Appendix A

This section illustrates the analytical derivation of the stability criterion for unsaturated soil samples under loading paths imposed by controlling net stresses and suction. In single-surface isotropic hardening plasticity models formulated in terms of Bishop's effective stresses, the Prager's consistency condition expresses as follows:

$$\frac{\partial f}{\partial \sigma'}^T \dot{\sigma}' + \frac{\partial f}{\partial \Psi}\dot{\Psi} = 0 \tag{A.1}$$

Where $\dot{\Psi}$ is defined as follows:

$$\dot{\Psi} = \frac{\partial \Psi}{\partial \varepsilon^p}\dot{\varepsilon}^p + \frac{\partial \Psi}{\partial S_r}\dot{S}_r \tag{A.2}$$

$\dot{\varepsilon}^p$ denotes the plastic strain increment tensor controlled by the flow rule:

$$\dot{\varepsilon}^p = \dot{\gamma}\frac{\partial g}{\partial \sigma'} \tag{A.3}$$

By substituting Eq, (A.2) and (A.3) in Eq. (A.1), the latter can be rewritten as follows:

$$\dot{f} := \frac{\partial f}{\partial \boldsymbol{\sigma}'}^T \dot{\boldsymbol{\sigma}}' + \frac{\partial f}{\partial \Psi}\left(\dot{\gamma}\frac{\partial \Psi}{\partial \boldsymbol{\varepsilon}^p}\frac{\partial g}{\partial \boldsymbol{\sigma}'} + \frac{\partial \Psi}{\partial S_r}\dot{S}_r\right) = 0 \tag{A.4}$$

Equation (A.4) can be simplified in the form:

$$\dot{f} := \frac{\partial f}{\partial \sigma'}^T \dot{\sigma}' - \dot{\gamma} H + \frac{\partial f}{\partial \Psi} \frac{\partial \Psi}{\partial S_r} \dot{S}_r = 0 \tag{A.5}$$

By introducing the hardening modulus H defined as:

$$H = -\frac{\partial f}{\partial \Psi} \frac{\partial \Psi}{\partial \varepsilon^p} \frac{\partial g}{\partial \boldsymbol{\sigma}'} \tag{A.6}$$

Bearing in mind that $\dot{\boldsymbol{\sigma}}' = \dot{\boldsymbol{\sigma}} + \left(\dot{s} S_r + \dot{S}_r s\right)\boldsymbol{\delta}$, Eq. (A.5) can be rearranged as follows:

$$\dot{f} := \frac{\partial f}{\partial \boldsymbol{\sigma}'}^T \dot{\boldsymbol{\sigma}} + \frac{\partial f}{\partial \boldsymbol{\sigma}'}^T \left(\dot{s} S_r + \dot{S}_r s\right)\boldsymbol{\delta} - \dot{\gamma} H + \frac{\partial f}{\partial \Psi} \frac{\partial \Psi}{\partial S_r} \dot{S}_r = 0 \tag{A.7}$$

Assuming an uncoupled retention behavior, Eq. (A.7) can be rewritten in the following form (since $\dot{S}_r = \frac{\partial S_r}{\partial s}\dot{s}$):

$$\dot{f} := \frac{\partial f}{\partial \boldsymbol{\sigma}'}^T \dot{\boldsymbol{\sigma}} + \frac{\partial f}{\partial \boldsymbol{\sigma}'}^T \left(\dot{s} S_r + \frac{\partial S_r}{\partial s} \dot{s} s\right)\boldsymbol{\delta} - \dot{\gamma} H + \frac{\partial f}{\partial \Psi} \frac{\partial \Psi}{\partial S_r} \frac{\partial S_r}{\partial s} \dot{s} = 0 \tag{A.8}$$

which corresponds to:

$$\dot{f} := \frac{\partial f}{\partial \boldsymbol{\sigma}'}^T \dot{\boldsymbol{\sigma}} - \dot{\gamma} H + \left(\frac{\partial f}{\partial \boldsymbol{\sigma}'}^T \left(S_r + \frac{\partial S_r}{\partial s} s\right)\boldsymbol{\delta} + \frac{\partial f}{\partial \Psi} \frac{\partial \Psi}{\partial S_r} \frac{\partial S_r}{\partial s}\right) \dot{s} = 0 \tag{A.9}$$

Given that the factor multiplying the rate of suction coincides to the partial derivative of yield surface with respect to suction, Eq (A.9) can be rewritten as:

$$\dot{f} := \frac{\partial f}{\partial \boldsymbol{\sigma}'}^T \dot{\boldsymbol{\sigma}} - \dot{\gamma} H + \frac{\partial f}{\partial s} \dot{s} = 0 \tag{A.10}$$

and, thus, the plastic multiplier results:

$$\dot{\gamma} = \frac{1}{H} \left\langle \frac{\partial f}{\partial \boldsymbol{\sigma}'}^T \dot{\boldsymbol{\sigma}} + \frac{\partial f}{\partial s} \dot{s} \right\rangle \tag{A.11}$$

Along stress paths activating plastic strains, positive values of the hardening modulus guarantees the uniqueness and existence of the soil response.

Appendix B

This section illustrates the analytical derivation of the stability criterion for unsaturated soil samples loaded under net stress-water content control conditions. In this case, the Prager's consistency condition expressed in Eq. (A.7) can be rewritten as follows:

$$\dot{f} := \frac{\partial f}{\partial \boldsymbol{\sigma}'}^T \dot{\boldsymbol{\sigma}} - \dot{\gamma} H + \frac{\partial f}{\partial S_r} \dot{S}_r = 0 \tag{B.1}$$

Being $\partial f / \partial S_r$ the partial derivative of the yield locus with respect to S_r defined in Eq. (12) and $\dot{S}_r$ linked to $\dot{e}_w$ and volumetric strain increment $\dot{\varepsilon}_v$ from the relationship:

$$\dot{e}_w = \dot{S}_r e + S_r \dot{e}; \dot{S}_r = \frac{1-n}{n} \dot{e}_w + \frac{S_r}{n} \dot{\varepsilon}_v \tag{B.2}$$

The volumetric strain increment is given by the sum of the elastic and plastic components:

$$\dot{\varepsilon}_v = \dot{\varepsilon}_v^e + \dot{\varepsilon}_v^p = (\boldsymbol{C}^e \dot{\boldsymbol{\sigma}}')^T \boldsymbol{\delta} + \dot{\gamma} \frac{\partial g}{\partial \boldsymbol{\sigma}'}^T \boldsymbol{\delta} \tag{B.3}$$

Bering in mind the definition of $\dot{\boldsymbol{\sigma}}'$, Eq. (B.3) can be rewritten in the form:

$$\dot{\varepsilon}_v = (\boldsymbol{C}^e \dot{\boldsymbol{\sigma}})^T \boldsymbol{\delta} + \left(\boldsymbol{C}^e \left(s + \frac{\partial s}{\partial S_r} S_r\right) \dot{S}_r \boldsymbol{\delta}\right)^T \boldsymbol{\delta} + \dot{\gamma} \frac{\partial g}{\partial \boldsymbol{\sigma}'}^T \boldsymbol{\delta} \tag{B.4}$$

By substituting Eq. (B.4) in Eq. (B.2):

$$\dot{S}_r = \frac{1-n}{n} \dot{e}_w + \frac{S_r}{n} \left[(\boldsymbol{C}^e \dot{\boldsymbol{\sigma}})^T \boldsymbol{\delta} + \left(\boldsymbol{C}^e \left(s + \frac{\partial s}{\partial S_r} S_r\right) \dot{S}_r \boldsymbol{\delta}\right)^T \boldsymbol{\delta} + \dot{\gamma} \frac{\partial g}{\partial \boldsymbol{\sigma}'}^T \boldsymbol{\delta}\right] \tag{B.5}$$

It, thus, follows that:

$$\dot{S}_r = \frac{\frac{1-n}{n}\dot{e}_w + \frac{S_r}{n}(\boldsymbol{C}^e\dot{\boldsymbol{\sigma}})^T\boldsymbol{\delta} + \frac{S_r}{n}\dot{\gamma}\frac{\partial g}{\partial \sigma'}^T\boldsymbol{\delta}}{\left(1 - \frac{S_r}{n}C^e_{pp}\left(s + \frac{\partial s}{\partial S_r}S_r\right)\right)} \tag{B.6}$$

By substituting the expression of $\dot{S}_r$ in the consistency condition, the latter modifies as follows:

$$\dot{f} := \frac{\partial f}{\partial \boldsymbol{\sigma}'}^T\dot{\boldsymbol{\sigma}} - \dot{\gamma}H + \frac{\partial f}{\partial S_r}\frac{\frac{1-n}{n}\dot{e}_w + \frac{S_r}{n}(\boldsymbol{C}^e\dot{\boldsymbol{\sigma}})^T\boldsymbol{\delta} + \frac{S_r}{n}\dot{\gamma}\frac{\partial g}{\partial \sigma'}^T\boldsymbol{\delta}}{\left(1 - \frac{S_r}{n}C^e_{pp}\left(s + \frac{\partial s}{\partial S_r}S_r\right)\right)} = 0 \tag{B.7}$$

Equation (B.7) can be simplified by introducing the definitions of $\overline{n}_{S_r}$ (see Eq. (11)) and $\overline{n}_\sigma$ (see Eq. (10)):

$$\dot{f} := \overline{n}_\sigma^T\dot{\boldsymbol{\sigma}} - \dot{\gamma}H + \overline{n}_{S_r}\left(\frac{1-n}{n}\dot{e}_w + \frac{S_r}{n}\dot{\gamma}\frac{\partial g}{\partial \sigma'}^T\boldsymbol{\delta}\right) = 0 \tag{B.8}$$

Accounting for the definition of H_w (see Eq. (13)), Eq. (B.8) can be rearranged as follows:

$$\dot{f} := \overline{n}_\sigma^T\dot{\boldsymbol{\sigma}} - \dot{\gamma}(H - H_w) + \overline{n}_{S_r}\frac{1-n}{n}\dot{e}_w = 0 \tag{B.9}$$

In conclusion, in shearing process under undrained conditions and water injection under constant total stresses, the uniqueness and existence of the incremental response is guaranteed by hardening moduli greater than H_w.

Appendix C

In this section, the stability criterion related to water content and net stress-controlled conditions is specialized to the WR2-Unsat model. Accounting for the isotropic hardening law, Eq. (14) reads as:

$$-\frac{\partial f}{\partial p_c}\frac{p_c}{\lambda^*}\frac{\partial g}{\partial p'} - \frac{\left[\frac{\partial f}{\partial p'}\left(s + \frac{\partial s}{\partial S_r}S_r\right) - \frac{\partial f}{\partial p_c}b p_c\right]}{\left[1 - \frac{S_r}{n}C^e_{pp}\left(s + \frac{\partial s}{\partial S_r}S_r\right)\right]}\frac{\partial g}{\partial p'}\frac{S_r}{n} \leq 0 \tag{C.1}$$

Assuming a diagonal elastic stiffness matrix and placing $C^e_{pp} = 1/K$:

$$-\frac{\partial f}{\partial p_c}\frac{p_c}{\lambda^*}\frac{\partial g}{\partial p'} - \frac{\left[\frac{\partial f}{\partial p'}\left(s + \frac{\partial s}{\partial S_r}S_r\right) + \frac{\partial f}{\partial p_c}b p_c\right]}{\left[1 - \frac{1}{K}\frac{S_r}{n}\left(s + \frac{\partial s}{\partial S_r}S_r\right)\right]}\frac{\partial g}{\partial p'}\frac{S_r}{n} \leq 0 \tag{C.2}$$

Eq. (C.2) can be simplified as follows (since $1 - S_r/nK(s + S_r\partial s/\partial S_r) \neq 0$):

$$-\frac{\partial f}{\partial p_c}\frac{p_c}{\lambda^*}\frac{\partial g}{\partial p'}\left[1 - \frac{1}{K}\frac{S_r}{n}\left(s + \frac{\partial s}{\partial S_r}S_r\right)\right] - \left[\frac{\partial f}{\partial p'}\left(s + \frac{\partial s}{\partial S_r}S_r\right) - \frac{\partial f}{\partial p_c}b p_c\right]\frac{S_r}{n}\frac{\partial g}{\partial p'} \leq 0 \tag{C.3}$$

On the wet side where $\partial g/\partial p' \geq 0$, Eq. (C.3) can be rearranged in the form:

$$-\frac{\partial f}{\partial p_c}\frac{p_c}{\lambda^*} - \left[\left(\frac{\partial f}{\partial p'} - \frac{\partial f}{\partial p_c}\frac{p_c}{\lambda^*}\frac{1}{K}\right)\left(s + \frac{\partial s}{\partial S_r}S_r\right) - \frac{\partial f}{\partial p_c}b p_c\right]\frac{S_r}{n} \leq 0 \tag{C.4}$$

From which derives the stability criterion reported in Eqs.(23), (25).

References

Amorosi, A., Rollo, F., Houlsby, G.T., 2020. A nonlinear anisotropic hyperelastic formulation for granular materials: comparison with existing models and validation. Acta Geotech. 15, 179–196. https://doi.org/10.1007/s11440-019-00827-5.

Benson, C.H., Chiang, I., Chalermyanont, T., Sawangsuriya, A., 2014. Estimating van Genuchten parameters α and n for clean sands from particle size distribution data. Geo-Congress 2014, 410–427.

Bigoni, D., Hueckel, T., 1991a. Uniqueness and localization – I. Associative and non-associative elastoplasticity. Int. J Solids Struct. 28, 197–213.

Bigoni, D., Hueckel, T., 1991b. Uniqueness and localization – II. Coupled elastoplasticity. Int. J Solids Struct. 28, 215–224.

Bigoni, D., Piccolroaz, A., 2004. Yield criteria for quasibrittle and frictional materials. Int J Solids Struct. 41, 2855–2878.

Boldini, D., Palmieri, F., Amorosi, A., 2019. A new versatile constitutive law for modelling the monotonic response of soft rocks and structured fine-grained soils. Int J Numer Anal Methods Geomech. 43 (15), 2383–2406.

Bui, H.H., Fukagawa, R., Sako, K., Ohno, S., 2008. Lagrangian meshfree particles method (SPH) for large deformation and failure flows of geomaterial using elastic–plastic soil constitutive model. Int J Numer Anal Methods Geomech. 32 (12), 1537–1570.

Bui, H.H., Nguyen, G.D., 2021. Smoothed particle hydrodynamics (SPH) and its applications in geomechanics: From solid fracture to granular behaviour and multiphase flows in porous media. Comput. Geotech. 138, 104315.

Buscarnera, G., Dattola, G., di Prisco, C., 2011. Controllability, uniqueness and existence of the incremental response: A mathematical criterion for elastoplastic constitutive laws. Int. J. Solids Struct. 48 (13), 1867–1878.
Buscarnera, G., di Prisco, C., 2013. Soil stability and flow slides in unsaturated shallow slopes: can saturation events trigger liquefaction processes? Géotechnique. 63 (10), 801–817.
Buscarnera, G., 2014. Uniqueness and existence in plasticity models for unsaturated soils. Acta Geotech. 9, 313–327 (2014).
Cascini, L., Cuomo, S., Sorbino, G., 2005. Flow-like mass movements in pyroclastic soils: remarks on the modelling of triggering mechanisms. RIG 4, 11–31.
Cascini, L., Cuomo, S., Guida, D., 2008. Typical source areas of May 1998 flow-like mass movements in the Campania region, Southern Italy. Eng. Geol. 96, 107–125.
Cattaneo, F., Della Vecchia, G., e Jommi, C., 2014. Evaluation of numerical stress-point algorithms on elastic–plastic models for unsaturated soils with hardening dependent on the degree of saturation. Comput. Geotech 55, 404–415.
Cevasco, A., Brandolini, P., Scopesi, C., Rellini, I., 2013. Relationships between geohydrological processes induced by heavy rainfall and land use: the case of 25 October 2011 in the Vernazza catchment (Cinque Terre, NW Italy). J. Maps. 9 (2), 289–298.
Chen, Y., Buscarnera, G., 2022. Unified modelling framework of flowslide triggering and runout. Géotechnique 1–14.
Chu, J., Leroueil, S., Leong, W.K., 2003. Unstable behaviour of sands and its implications for slope instability. Can. Geotech. J. 40 (5), 873–885.
Comegna, L., Damiano, E., Greco, R., Guida, A., Olivares, L., Picarelli, L., 2016. Field hydrological monitoring of a sloping shallow pyroclastic deposit. Can. Geotech. J. 53 (7), 1125–1137.
Cuomo, S., 2020. Modelling of flowslides and debris avalanches in natural and engineered slopes: a review. Geoenviron Disasters. 7 (1).
Cuomo, S., Di Perna, A., Martinelli, M., 2021. Modelling the spatio-temporal evolution of a rainfall-induced retrogressive landslide in an unsaturated slope, Eng. Geol., 294, 5 December 2021, 106371.
Cuomo, S., Moscariello, M., Foresta, V., 2017. Wetting tests of partially saturated soils under simple shear conditions. Géotechnique Letters 7 (2), 197–203.
Cuomo, S., Ghasemi, P., Martinelli, M., Calvello, M., 2019. Simulation of liquefaction and retrogressive slope failure in loose coarse-grained material. Int. J. Geomech. 19 (10), 04019116.
Dai, F.C., Lee, C.F., Wang, S.J., 1999. Analysis of rainstorm-induced slide-debris flows on natural terrain of Lantau Island Hong Kong. Eng. Geol. 51, 279–290.
Damiano, E., 2003. Meccanismi d'innesco di colate di fango in terreni piroclastici. Second University of Naples, Naples, Italy. Ph.D. thesis,.
Damiano, E., Olivares, L., Picarelli, L., 2012. Steep-slope monitoring in unsaturated pyroclastic soils. Eng. Geol. 137–138, 1–12.
Fuchu, D., Lee, C.F., Sijing, W., 1999. Analysis of rainstorm induced slide-debris flows on natural terrain of Lantau Island, Hong Kong. Eng. Geol. 51, 279–290.
Gallage, C.P.K., Uchimura, T., 2010. Effects of dry density and grain size distribution on soil–water characteristic curves of sandy soils. Soils and Foundations. 50 (1), 161–172.
Gallipoli, D., Gens, A., Sharma, R., Vaunat, J., 2003. An elasto-plastic model for unsaturated soil incorporating the effects of suction and degree of saturation on mechanical behavior. Géotechnique. 53 (1), 123–135.
Gallipoli, D., Gens, A., Chen, G., D'Onza, F., 2008. Modelling unsaturated soil behaviour during normal consolidation and at critical state. Comput. Geotech. 35 (6), 825–834.
Hardin, B.O., Black, W.L., 1966. Sand stiffness under various triaxial stresses". Journal of the Soil Mechanics and Foundations Division. 2 (2), 27–42.
Hou, X., Vanapalli, S.K., Li, T., 2019. Wetting-induced collapse behavior associated with infiltration: A case study. Eng. Geol. 258, 105146.
Houlsby, G.T., Amorosi, A., Rojas, E., 2005. Elastic moduli of soils dependent on pressure: a hyperelastic formulation. Géotechnique 55 (5), 383–392.
Hueckel, T., Maier, G., 1977. Incremental boundary value problems in the presence of coupling of elastic and plastic deformations: a rock mechanics oriented theory. Int. J. Solids Struct. 13, 1–15.
Jefferies, M., Been, K., 2015. Soil Liquefaction: A Critical State Approach, Second Edition, 2nd ed. CRC Press, New York.
Lalicata, L.M., Rotisciani, G.M., Desideri, A., Casini, F., Thorel, L., 2020. Physical modelling of piles under lateral loading in unsaturated soils. E3S Web Conf. 195, 01021.
Laloui, L., Ferrari A., Bonnard, C., 2009. Geomechanical modeling of the Steinernase landslide (Switzerland). In Proceedings of the 1st Italian Workshop on Landslides, June 8–10, Naples, Italy, 186–195.
Lian, Y., Bui, H.H., Nguyen, G.D., Zhao, S., Haque, A., 2022. A computationally efficient SPH framework for unsaturated soils and its application to predicting the entire rainfallinduced slope failure process. Géotechnique. 1–60.
Likos, W.J., Lu, N., Godt, J.W., 2014. Hysteresis and uncertainty in soil water-retention curve parameters. J. Geotech. Geoenviron. Eng. 140 (4) https://doi.org/10.1061/(ASCE)GT.1943-5606.0001071.
Lo Presti, D. C., 1989. Proprietà dinamiche dei terreni. Proc. XIV CGT, 2, 1-62, Politecnico di Torino *(in Italian)*.
Maier, G., Hueckel, T., 1979. Non-associated and coupled flow-rules of elastoplasticity for rock-like materials. Int. J. Rock. Mech. Min. Sci. 16, 77–92.
Mihalache, C., Buscarnera, G., 2014. Mathematical identification of diffuse and localized instabilities in fluid-saturated sands. Int. J. for Numer. Anal. Meth. Geomech. 38 (2), 111–141.
Montrasio, L., Valentino, R., 2008. A model for triggering mechanisms of shallow landslides. Nat. Hazards Earth Syst. Sci. 8, 1149–1159.
Moriwaki, H., Inokuchi, T., Hattanji, T., Sassa, K., Ochiai, H., Wang, G., 2004. Failure processes in a full-scale landslide experiment using a rainfall simulator. Landslides 1, 277–288.
Ng, C.W., Crous, P.A., Zhang, M., Shakeel, M., 2022. Static liquefaction mechanisms in loose sand fill slopes. Comput. Geotech. 141, 104525.
Nguyen, L.C., Tien, P.V., Do, T.N., 2020. Deep-seated rainfall-induced landslides on a new expressway: a case study in Vietnam. Landslides 17, 395–407.
Nicotera, M.V., Papa, R., Urciuoli, G., 2015. The hydro-mechanical behaviour of unsaturated pyroclastic soils: an experimental investigation. Eng. Geol. 195, 70–84.
Oh, W.T., Vanapalli, S.K., 2010. Influence of rain infiltration on the stability of compacted soil slopes. Comput. Geotech. 37 (5), 649–657.
Okura, Y., Kitahara, H., Ochiai, H., Sammori, T., Kawanami, A., 2002. Landslide fluidization process by flume experiments. Eng. Geol. 66, 65–78.
Olivares, L., Damiano, E., 2007. Postfailure mechanism of landslides: laboratory investigation of flowslides in pyroclastic soils. J. Geotech. Geoenviron. Eng. 133 (1), 51–62.
Olson, S.M., Mattson, B.B., 2008. Mode of shear effects on yield and liquefied strength ratios. Can. Geot. J. 45 (4), 574–587. https://doi.org/10.1139/T07-114.
Olson, S.M., Stark, T.D., 2003. Use of laboratory data to confirm yield and liquefied strength ratio concepts. Can. Geot. J. 40 (6), 1161–1184.
Pastor, M., Blanc, T., Pastor, M.J., 2009. A depth-integrated viscoplastic model for dilatant saturated cohesive-frictional fluidized mixtures: Application to fast catastrophic landslides. J. Non-Newton. Fluid Mech. 158 (1–3), 142–153.
Picarelli, L., Olivares, L., Comegna, L., Damiano, E., 2008. Mechanical Aspects of Flow-Like Movements in Granular and Fine Grained Soils. Rock Mech. Rock Engng. 41 (1), 179–197.
Pirone, M., Papa, R., Nicotera, M.V., Urciuoli, G., 2015. In situ monitoring of the groundwater field in an unsaturated pyroclastic slope for slope stability evaluation. Landslides. 12 (2), 259–276.
Rotisciani, G.M., Sciarra, G., Desideri, A., Casinit, F., 2014. Modeling rainfall infiltration through coarse and fine-grained unsaturated geomaterials. Unsaturated Soils: Research & Applications, CRC Press 521–528. https://doi.org/10.1201/b17034-73.
Rotisciani, G.M., Casini, F., Desideri, A., Sciarra, G., 2017. Hydromechanical behavior of an embankment during inundation. Can. Geot. J. 54 (3), 348–358.
Rotisciani, G.M., di Prisco, C., Desideri, A., 2019. Numerical analysis of wetting-induced instabilities in partially saturated soils under plane strain conditions. Int J Numer Anal Methods Geomech. 43 (10), 1867–1884.
Rotisciani, G.M., Lalicata, L.M., Desideri, A., Casini, F., 2020. Numerical modelling of the response of an unsaturated silty soil under wetting and gravitational loading processes. E3S Web Conf. 195, 02012.
Rotisciani, G.M., Desideri, A., Amorosi, A., 2021. Unsaturated structured soils: constitutive modelling and stability analyses. Acta Geotech. 16, 3355–3380.
Rotisciani, G.M., Desideri, A., Amorosi, A., 2023. A new constitutive model for cemented unsaturated soils: model performance and stability analysis. Proceedings 10th NUMGE, Zdravkovic L, Kontoe S, Taborda DMG, Tsiampousi A (eds), Doi: 10.53243/NUMGE2023-319.
Salciarini, D., Godt, J.W., Savage, W.Z., Conversini, P., Baum, R.L., Michael, J.A., 2006. Modeling regional initiation of rainfall-induced shallow landslides in the eastern Umbria Region of central Italy. Landslides 3, 181–194.
Seed, H.B., Wong, R.T., Idriss, I.M., Tokimatsu, K., 1986. Moduli and damping factors for dynamic analyses of cohesionless soils". J. Geotech. Eng. 112 (11), 1016–1032.
Sorbino, G., Nicotera, M.V., 2013. Unsaturated soil mechanics in rainfall-induced flow landslides. Eng. Geol. 165, 105–132.
Springman, S.M., Thielen, A., Kienzler, P., Friedel, S., 2013. A long-term field study for the investigation of rainfall-induced landslides. Geotechnique. 63 (14), 1177–1193.
Tayyebi, S.M., Pastor, M., Stickle, M.M., Yagüe, Á., Manzanal, D., Molinos, M., Navas, P., 2022. SPH numerical modelling of landslide movements as coupled two-phase flows with a new solution for the interaction term, Eur. J. Mech. B, Fluids 96, 1–14.
Wang, G., Sassa, K., 2001. Factors affecting rainfall-induced flowslides in laboratory flume tests. Geotechnique. 51 (7), 587–599.
Wang, G., Sassa, K., 2003. Pore-pressure generation and movement of rainfall induced landslides: effects of grain size and fine-particle content. Eng. Geol. 69, 109–125.
Weng, X., Sun, Y., Zhang, Y., Niu, H., Liu, X., Dong, Y., 2019. Physical modeling of wetting-induced collapse of shield tunneling in loess strata. Tunnelling and Underground Space Technology. 90, 208–219.
Wong, K.S., Mašín, D., Ng, C.W.W., 2014. Modelling of shear stiffness of unsaturated fine-grained soils at very small strains. Comput. Geotech. 56, 28–39.
Wu, L.Z., Huang, J., Fan, W., Li, X., 2020. Hydro-mechanical coupling in unsaturated soils covering a non-deformable structure. Comput. Geotech. 117, 103287.
Yang, H., Yang, T., Zhang, S., Zhao, F., Hu, K., Jiang, Y., 2020. Rainfall-induced landslides and debris flows in Mengdong Town, Yunnan Province, China. Landslides. 17, 931–941 (2020).
Zizioli, D., Meisina, C., Valentino, R., Montrasio, L., 2013. Comparison between different approaches to modelling shallow landslide susceptibility: a case history in Oltrepò Pavese, Northern Italy. Nat. Hazards Earth Syst. Sci. 13, 559–573.
Zlatović, S., Ishihara, K., 1998. Flow failure - some data on onset conditions. Geotechnical Hazards, Marić, Lisac & Szavits-Nossan (eds), Balkema, Rotterdam, 385-389.
Zlatović, S., Ishihara, K., 1997. Normalized behavior of very loose non-plastic soils: effects of fabric. Soils and Foundations. 37 (4), 47–56.